ECS Journal of Solid State
Science and Technology

Critical Review—A Promising Cs_3CoCl_5 Prototype Phosphor toward the Discovery of Next-Generation LED Phosphor

Review—A Promising Cs_3CoCl_5 Prototype Phosphor toward the Discovery of Next-Generation LED Phosphor

N. S. M. Viswanath,[1] Jun Hyeong In,[2] Ha Jun Kim,[2] G. Krishnamurthy Grandhi,[2] and Won Bin Im[2,z]

[1]*School of Materials Science and Engineering, Chonnam National University, Buk-gu, Gwangju, 61186 Korea*
[2]*Division of Materials Science and Engineering, Hanyang University, Seongdong-gu, Seoul, 04763 Korea*

To improve and identify next-generation solid-state lighting devices, there is an urgent need to discover new and highly efficient phosphor materials. Currently, the preparation of phosphor materials is considered to be an art rather than science and is based on finding crystal structures that can act as hosts for the activator ions. Thus far, there has been no systematic analysis on how to select host structures for given activator ions such that the synthesized phosphor is efficient. In this review, the general strategies for tuning and enhancing the photoluminescence properties of phosphor materials for white light-emitting diodes are discussed with respect to versatile host materials belonging to the Cs_3CoCl_5 family. Furthermore, we also discuss several important parameters for constructing the sort diagram for selecting efficient host materials.
 [DOI: 10.1149/2.0232001JSS]

Manuscript submitted July 31, 2019; revised manuscript received September 19, 2019. Published October 29, 2019. *This paper is a Critical Review in Electrochemical and Solid State Science and Technology* (*CRES*^{3}*T*). *This article was reviewed by Anant Setlur (setlur@ge.com). This paper is part of the JSS Focus Issue on Recent Advances in Wide Bandgap III-Nitride Devices and Solid State Lighting: A Tribute to Isamu Akasaki.*

In the current state, white light-emitting diodes (WLEDs) are counted upon as a mature technology that can contend with traditional incandescent and fluorescent lamps. They have many advantages when compared to the latter, such as high luminescence efficiency, low power consumption, high lifetime, reliability, robustness, and environmental friendliness. It is well known that replacing incandescent lamps with high-efficiency light sources can reduce electricity consumption, corresponding to the energy produced about 140 power plants of average size in the US alone, for a 40% market penetration and luminous efficacy of 150 lm/W.[1] However, LEDs face several disadvantages, such as their need for extensive cooling for high-power devices, current driving requirements, and lack of a high color rendering index (CRI) in WLEDs. Hence, it is critical to develop new-generation LED technologies using new inorganic phosphor materials. The most suitable phosphors for this application involve the broad and spin allowed 4*f* and 5*d* transitions of Ce^{3+} and Eu^{2+} ions that are substituted in host materials,[2] as 4*f* and 5*d* transistors are strongly influenced by the crystal field splitting of 5*d* energy levels. Hence, the crystal geometry and chemistry of host lattices is a significant parameter for choosing new host materials.

Recently, material scientists are paying much attention to the development of new inorganic phosphor materials by the chemical substitution of known compounds and using computational techniques (Figure 1). Recently, Horky et al.[3] synthesized an oxonitridosilicate fluoride phosphor by co-doping F into $Li_2SrSi_2N_4$ to form a new host compound of $Li_{24}Sr_{12}[Si_{24}N_{47}O]F$; this host material exhibited orange-red luminescence under blue light excitation. In addition, Maak et al.[4] developed two oxynitride silicate phosphors of $Lu_4Ba_2[Si_9ON_{16}]O:Eu^{2+}$ and $Y_4Ba_2[Si_9ON_{16}]O:Eu^{2+}$ that exhibited orange-red and yellow-orange luminescence, respectively, with a high photoluminescence quantum yield (PLQY) of 85%. Elzer et al.[5] discovered that beryllium-containing nitride phosphors of $MBe_{20}N_{14}$ (M = Ca and Sr) exhibits two emission bands in the blue to green spectral region.

Wang et al.,[6] Gregor et al.,[7] and Zhuo et al.[8] employed machine learning technology to develop superior performing phosphors of $Sr_2LiAlO_4:Eu^{2+}$, $Sr[Li_2Al_2O_2N_2]:Eu^{2+}$, and $NaBaB_9O_{15}:Eu^{2+}$ that exhibit green, red, and blue spectral regions, respectively, with a high PLQY. Meanwhile, Park et al.[9–13] used combinatorial chemistry and high-throughput approaches and reported several nitride phosphors for WLED applications. Although the above-mentioned approaches show much promise, the success rate of developing new phosphor materials is very low from the application point of view. Hence, a set of guide-lines is necessary to discover efficient and targeted compositions similar to those of organic LEDs and metal-organic frame works. For example, phenolphthalein, an organic dye, does not show any fluorescence due to quenching, which can be attributed to the high rotational degree of freedom of its phenyl rings.[14,15] However, once the phenyl rings are constrained by bridging oxygen ions, the crystal rigidity of the dye increases and it quenches nonradiative relaxation pathways, leading to a high PLQY.[16] However, in the solid state, it is highly difficult to design useful rules due to the complex nature of inorganic phosphor materials. Therefore, we need to focus on developing material descriptors (proxies) rather than framing new rules.[17–20] For example, the yttrium aluminum garnet ($Y_3Al_5O_{12}$; YAG) crystal structure contains two sublattices, one containing AlO_4 tetrahedra and AlO_6 octahedra and the second containing Y^{3+} ions. These networks lead to an interpenetrating three-dimensional connectivity that makes YAG very rigid. However, the connectivity of other oxide phosphor

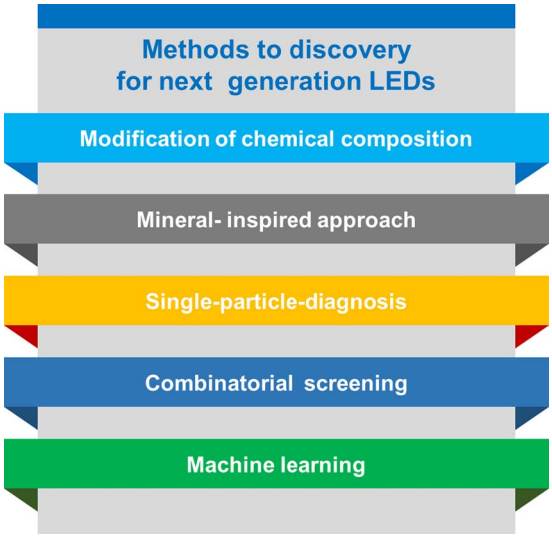

Figure 1. The general approaches to discover the new LED phosphors; the methods include modification of chemical composition, combinatorial screening, single-particle diagnosis, mineral inspired approach, and machine learning respectively.

[z]E-mail: imwonbin@hanyang.ac.kr

hosts, such as yttrium silicates, Y_2SiO_5 and β-$Y_2Si_2O_7$ (apart from SiO_4 tetrahedra), are not self-evident, which makes structural comparison difficult. A more appropriate method for determining rigidity is to evaluate the Debye temperature of the host crystal. A large value indicates that a structure is not only (vibrationally) rigid but also highly connected. Let us consider diamond as a prototypical example; it has a Debye temperature of 1860 K, while graphite has an in-plane (sheet) and out-of-plane (between sheets) Debye temperature of 2500 and 950 K, respectively, due to anisotropic bonding in the structure. In the case of similar phosphor hosts, a large Debye temperature is indicative of a well-connected and rigid structure. Such high rigidity limits non-radiative relaxation pathways. Thus, it is likely that a large Debye temperature is a good predictor of high PLQY. Another essential parameter to achieve a high PLQY and good thermal stability is a wide host bandgap (E_g). One should note that crystal rigidity and wide E_g alone do not give any guarantee to develop the new efficient phosphors and the calculations involving these descriptors often fail to consider the interactions between the activator ion and its surroundings. To overcome this problem, it is needed to discover the new descriptors with features that are largely induced by the local environment of the activator ions, which largely influenced by the two important factors, one is crystal field splitting and centroid shift of the phosphor materials. Therefore, in the coming discussions, firstly we would like to explain the crystal field splitting and then finally elucidate the centroid shift of phosphor materials by considering various examples.

To understand the importance of crystal field splitting of phosphor materials, let us consider the examples of $Sr_2Si_5N_8$:Eu^{2+}, $BaSi_7N_{10}$:Eu^{2+}, and AlN:Eu^{2+}, Si^{4+} phosphors in an effort to understand how the geometry of the coordination polyhedron can be used to give a quick qualitative prediction toward the shift of emission wavelength.[21] By examining the local geometries of the crystal structure, it was found that the coordination number of Eu^{2+}dopant varies from 12 to 13 as proved in the hosts of AlN and $BaSi_7N_{10}$.The accessibility of large coordination numbers makes the Eu^{2+} ion loosely coordinated, leading to give a small centroid shift and crystal field splitting. The decreased redshift observed for $BaSi_7N_{10}$ and AlN hosts is solely responsible for the emission of Eu^{2+} at a wavelength shorter than that in the $Sr_2Si_5N_8$ host lattice. Meijerink and co-workers thoroughly studied the emission of Eu^{2+} ions incorporated in a series of strontium aluminates.[22] Similarly, they found that the increase in coordination number certainly leads to a reduced centroid shift and crystal field splitting and ultimately a short emission wavelength. This perception also holds good for $Y_3Al_{5-x}Ga_xO_{12}$:Ce^{3+} phosphors in which the blue shifts in both excitation and emission spectra originate from a less distorted coordination polyhedron around Ce^{3+}. Conversely, an increased distortion of the coordination polyhedron usually increase a crystal field splitting in the 4*f*-5*d* transition, as exemplified in Y_3Al_{5-x}(Mg, Si)$_xO_{12}$:Ce^{3+} and $CaSrSi_{1-x}Al_xO_4$:Ce^{3+}, Li^+ phosphors.[23] The accurate prediction of luminescent properties, however, remains challenging, largely due to the hypothetic nature of the lattice relaxation parameter. The splitting of the lanthanides 5*d* orbitals highly depends on the coordination environment. For example, within an octahedral coordination O_h geometry, the 5*d* orbitals can split into double degenerate high-energy levels and triple degenerate low-energy levels, while a reversed energy alignment is typically observed for a tetrahedral coordination T_d geometry. Extended X-ray absorption fine structure (EXAFS) experiments on Ce^{3+}-doped garnets are able to provide two Ce-O distances,[24] but the details of full structural parameters of the CeO_8 moiety remain unclear. It is thus a general practice for researchers to investigate optical properties of a material on the basis of undoped crystal structures. As such, the structural distortion induced by the mismatch in ionic radius between the dopant and the host cation is usually not included.

The second effect is the centroid shift, denotes to a lowering in the energy of the 5*d* levels of the activator ion due to a decrease in the interelectron repulsion. This effect depends on the polarizability of the surrounding anion (oxygen) ligands and on the covalency of the chemical bonds between the ligands and the activator ion as described in the Equations 1 to 3.[25,26]

$$\frac{\varepsilon_c}{N} = \frac{1.44 \times 10^7 \alpha_{sp}}{R_{eff}^6} \quad [1]$$

$$\frac{1}{R_{eff}^6} = \frac{1}{N} \sum_{i=1}^{n} \frac{1}{\left(R_i - \frac{1}{2}\Delta R\right)^6} \quad [2]$$

$$\alpha_{sp} = \alpha_0(x) + \frac{b(x)}{\chi_{av}^2} \quad [3]$$

where ε_c represents the centroid shift, N represents the coordinating anion ligands, α_{sp} represents the spectroscopic polarizability of anion i located at R_i, ΔR represents the size difference between the cation and luminescent center, and χ_{av}^2 represents the average electronegativity of the cations in the compound.

The centroid shift increases with increasing anion polarizability and decreasing average electronegativity of the host cations. As the degree of covalency between the activator ion and surrounding anions increases, the electrons of the metal ion are partly delocalized on the ligands and this decreases their interelectronic repulsion, therefore, decreasing the energy of the excited levels of the metal ion. This feature is called the nephelauxetic effect.

Furthermore, the energetics of the activator ions is determined by the Stokes shift, which refers to the difference in energy between the band maxima of the absorption and emission spectra. This can be understood by the use of a configurational coordinate diagram, in which the potential energy curves of the activator ion in the ground and excited state are plotted against a so-called configurational coordinate that represents the normal coordinate of a vibrational mode localized at the optical center. According to the Franck–Condon principle, the electronic transitions (absorption and emission) are vertical in nature and (at low temperature) occur from the lowest vibrational level. In effect, this means that once an electron is excited to the 5*d* level, the surrounding lattice first relaxes to the lowest vibrational level in the electronic excited state before the electron is de-excited to the electronic ground state. Since the Stokes shift requires the interaction with phonons, this property is also dictated by the host crystal. The phonons also play a key role in a phenomenon known as thermal quenching, which describes the pronounced reduction in emission intensity, or quantum efficiency, observed at elevated temperatures, typically a few hundred degree centigrade. Since LED chips produce heat, which may easily get transferred to the phosphor coating, this is of pivotal importance with respect to the energy efficiency of LED devices. On a fundamental level, thermal quenching relates to nonradiative relaxation mechanisms of the excited-state electron, other than concentration quenching that relates to the activation of energy processes involving the excited states of the Ln^{3+} ion and depopulating in a non-radiative way the light emitting levels. In the case of Ce^{3+} dopants, the two primary mechanisms are thought to be thermal promotion of the 5*d* electron to the conduction band of the host crystal, and 5*d*–4*f* crossover, regardless of the mechanism, phonons are needed to bring the excited activator ion to a point at which non-radiative processes can happen.

Furthermore, whereas in many an oxide hosts the activator ions occupy well-defined substitutional sites, predictable on the basis of simple arguments based on the charge and the size of the dopant and the substituted ions, this is not the case for all materials. A notable example of this behavior is the non-linear host $LiNbO_3$, which is of great interest for its ability to generate the second harmonic radiation of the light emitted from Ln^{3+} ions and for which the Ln^{3+} ions have a different charge with respect to the host cations (Li^+ and Nb^{5+}) and also a different ionic radius (Li^+ and $Nb^{5+}$are smaller than the Ln^{3+} ions). It is clear that in such cases the local structure around the activator ions is not easily predictable and the simultaneous occupation of multiple substitutional sites cannot be excluded. This situation occurs for many classes of host matrices of technological interest and in particular for garnet type host lattices, such as YAG, Moreover, it is well known that garnet crystals (in particular YAG) are subject to significant amounts of native defects that appear during crystal growth depending on the

temperature and crystallization procedure. Among these intrinsic defects, antisite defects are dominant. They appear in YAG when some Y and Al atoms exchange positions. The antisite defects are known to act as electron traps and to affect the structure, luminescence, and other properties of doped and undoped YAG. Moreover, in garnets not containing a large trivalent cation, such as $Ca_3Sc_2Si_3O_{12}$, the localization of the trivalent dopant is not generally trivial. It can be concluded that it is important to get more insight on this subject.

The location of the 5*d* band relative to 4*f* band also plays an important role, in order to develop the new phosphor materials with high PL efficiencies. Therefore, one should have the knowledge on the specific positions of the 4*f* and 5*d* levels relative to the host energy bands, qualitatively measure the occurrence of the 4*f*-5*d* transitions. Recently, a series of research activities have been implemented by Ibrahimand Benco and their co-workers in $LaSi_3N_5$-based phosphors to study the relative energy levels of 4*f* and 5*d* orbitals for Ce, Pr, Nd, Pm, Sm, and Eu dopants.[27] The researchers found that the lowest 4*f* energy levels can locate either above or in close proximity to the host valency band maximum, or deeply embedded in the host valence band. The unoccupied 4*f* energy levels were found to mostly locate at the bottom of the conduction band. Compared to the well-defined and localized 4*f* orbitals, the 5*d* orbitals of lanthanide ions are rather isolated and highly mixed with the conduction band. Interestingly, Watras and coworkers predicted that the 4*f*-5*d* transitions in a $KCa(PO_3)_3$ host could take place only within the ultraviolet spectral region when the Ca vacancy-mediated generation of Eu^{3+}occurs.[28] Their band structure calculations suggest the absence of 5*d*-4*f* transition of Eu^{2+}. Importantly, the theoretical results are consistent with the experimental data, which show the missing of Eu^{2+} emission bands. Therefore, the observed red light in the emission spectrum is most likely due to the 4*f*-4*f* transition of Eu^{3+}.

Similarly, $LaSi_3N_5$:Eu^{2+}[29] phosphor, the 4*f* and 5*d* energy levels are located within the E_g. Therefore, emission can occur from $LaSi_3N_5$ doped with divalent lanthanides as occupied 4*f* orbitals reside in the E_g. However, no luminescence could be observed experimentally with $LaSi_3N_5$:Eu^{2+}, which could be attributed to thermal quenching induced by the highly destabilized 5*d* states of divalent lanthanides. Recently, Tolhurst et al.[30] determined energy distance between the 5*d* band and conduction band maxima in $Sr[LiAl_3N_4]$:Eu^{2+}, $Sr[Mg_3SiN_4]$:Eu^{2+}, $LiCa_2[Mg_2Si_2N_6]$:Eu^{2+}, and $Ba[Li_2(Al_2Si_2)N_6]$:Eu^{2+} to be 0.20, 0.10, 0.47, and 0.37 eV, respectively. Among these phosphor materials, $LiCa_2[Mg_2Si_2N_6]$:Eu^{2+} had the largest distance between the 5*d* band and conduction band, which reflects a high thermal quenching property with low PLQY. Meanwhile, the PLQY of $CaBa[Li_2Al_6N_8]$:Eu^{2+} phosphors varies with temperature depending on the occupation of Eu^{2+} in cation sites. Ca-occupied Eu^{2+} shows only 58% PLQY, while a Ba-occupied activator exhibits 95% PLQY. This is because the mean phonon energy of the Ba site is lower than that of the Ca site.[31]

From the above-mentioned examples, it can be understood that the host material composition and location of the 5*d* band has the same importance compared to the Debye temperature, E_g, and to design the novel phosphor materials. Therefore, the Debye temperature, E_g, host-material composition, and location of the 5*d* band may be considered as the rule-of-thumb parameters to develop the potential phosphor hosts.

One particular series of phosphor hosts that show highly efficient emission properties belong to the class of alkaline-earth oxyfluorides. These structures are similar to Sr_3SiO_5 with isolated AlO_4 tetrahedra. In oxyfluorides, one of the O^{2-} ions is replaced with a F^- ion.

Sr_3SiO_5 exhibits three dimensionally connected features similar to those of YAG. The calculated Debye temperature and E_g of YAG are ~730 K and 4.5 eV, respectively. Sr_3SiO_5-type compounds exhibit a surprisingly large Debye temperature of ~465 K and an E_g of 4.5 eV, which is unexpected due to the presence of isolated AlO_4 and SiO_4 tetrahedra. It is also noted that local coordination around activation ions in these compounds is similar to that in YAG. Yet, the PLQY of such oxyfluorides is relatively similar to that of YAG phosphors. Having a very large E_g is clearly advantageous when considering thermal quenching; however, the location of the activation center should be considered to obtain better luminescence properties of the phosphor. Owing to their excellent luminescence properties and possibility of structural modification, Sr_3SiO_5-type phosphor materials have been considered as an example to construct sorting diagrams to develop novel LED phosphors.

This review is mainly focused on the structural and optical properties of the Cs_3CoCl_5 family for WLED applications. Firstly, important features related to the structural properties of the isostructural hosts belonging to this archetypal family are discussed. Later, the optical properties of rare-earth-substituted oxyfluoride phosphors are analyzed along with energy transfer process by co-activation with other rare-earth ions. Finally, the phase formation and luminescence properties of binary and ternary solid-solutions in tetragonal systems are discussed. In the conclusions section, we summarize the optical properties of the Cs_3CoCl_5 family for fabricating high-quality WLEDs. Currently, the number of high-performance conversion phosphors is still limited. Hence, we highlight possible future research directions for developing new phosphor materials for next-generation devices. We hope that this review draws the attention of the broader research community toward inorganic luminescent materials.

In order to develop and optimize the new phosphor materials, there are four strategies for matching phosphors to LED applications are:

1) Selection of crystal structure.
2) The modification of chemical composition by cation or anion substitution.
3) The modification of chemical composition by chemical unit co-substitution.
4) The coupling of activator ions into host lattice.
5) The design of energy transfer process.

In this regard, we have mainly focused on the strategy-1, strategy-2 and strategy-3 respectively.

Strategy-1: Selection of Crystal Structure

As mentioned earlier, there are two factors affecting the selection of an efficient host material the Debye temperature and E_g. Structures belonging to the Cs_3CoCl_5 family exhibit a large Debye temperature of ~465 K, which is unexpected due to the presence of isolated AlO_4 and SiO_4 tetrahedra in their structures. Further, they have a large E_g in the range of 4.5 to 4.7 eV. Hence, these structures fulfill the requirements of potential proxies for choosing new host materials for WLED applications.

In 1980s Drofenik, Kolar & Golic group proposed the group of alkaline-earth pentaoxometallates, with strontium replaced by rare earth elements. During their extensive work Scholder synthesized a series of isotypic compounds with the general formula Ba_3MO_5 (M = Ti, V, Cr, Mn, Fe, Co, Si, Ge). Later, Gotsmann and Letzelter prepared some ternary compounds Sr_2LaAlO_5 and Ba_2LaMO_5 (M = Mn, Fe, Co, A1, Ga). During their study of silicates, Dent Glasser solved the crystal structure of Sr_3SiO_5 and designated the structural relationship between Sr_3SiO_5, Cd_3SiO_5 and Ca_3SiO_5. Mansmann found that three barium pentaoxometallates Ba_3MO_5 were isotypic with Cs_3CoCl_5 (Powell & Wells, 1935), and reported that the structure of Sr_3SiO_5 (*P*4/*ncc*) is isotypic with Cs_3CoCl_5 (*I*4/*mcm*) up to the second non-metal position, which causes the transition from a centrosymmetric to a primitive lattice.

Sr_3SiO_5 (SSO), Sr_3AlO_4F (SAF), and $LaSr_2AlO_5$ (LSA) crystallize into a tetragonal phase with a space group of *P*4/*ncc* (number 130) and *I*4/*mcm* (number 140). These structures have similar structural features and are closely related to $Sr_3M^{4+}O_5$-type compounds.

In the SSO structure (Figure 2a), each unit cell consists of 12 strontium, 4 silicon, and 20 oxygen atoms. The strontium ions be inherent, and it occupies 8*f* and 4*c* sites respectively. The coordination between strontium atoms in this structure is approximately octahedral. It is interesting to note the distortion of the $Sr^{2+}(2)$ octahedron with five of six oxygen atoms crowed into the hemisphere. In a similar manner,

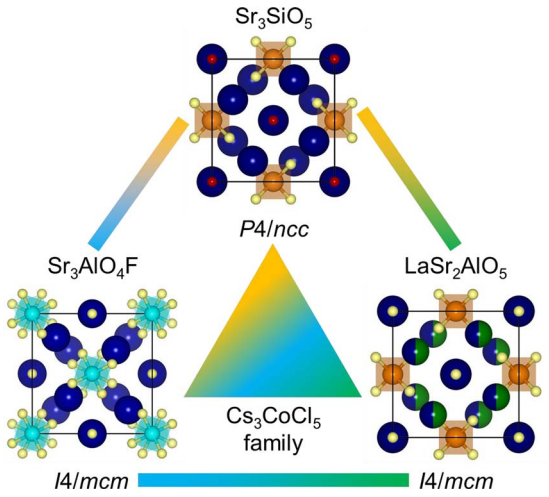

Figure 2. (a) Represents the crystal structure of SSO host in [001] direction. Blue, cyan, and yellow spheres showing the Sr, Si, and O atoms respectively. (b) represents the crystal structure of SAOF host in [001] direction. Blue, orange, yellow, and red spheres showing the Sr, Al, O, and F atoms respectively. (c) The crystal structure of LSA., with La/Sr1 at 8*h* (x, $x + 0.5$, 0) (blue spheres), Sr_2 at 4*a* (0, 0, 0.25) (green spheres), Al at 4*b* (0, 0.5, 0.25) (orange within Al(O2) 4 tetrahedra), O1 at 4*c* (0, 0, 0), O2 at 16*l* (x, $x + 0.5$, z) (small yellow spheres).

silicon atoms form a tetrahedron and they occupies the 4*b* site while O^{2-} ions occupy the 16*g* and 4*c* sites.

The SAF crystal structure (Figure 2b) belongs to the family of anion-ordered oxyfluorides with a general formula of $Sr_{3-x}A_xMO_4F$ (where A = Ca^{2+}, Ba^{2+}, and Sr^{2+} and M = Al^{3+} and Ga^{3+});[32–34] these oxyfluoride host lattices are responsive to iso-and aliovalent cation doping[35] and also show self-activating photoluminescence when synthesized in a reduction atmosphere. These structures consist of two discrete strontium cation sites, crystallizing in a layered structure alternating with isolated MO_4 tetrahedra with interposed to $Sr^{2+}(1)$ cations. The 10-coordinate $Sr^{2+}(1)$ site occupies 4*a* site positions while 8-coordinate $Sr^{2+}(2)$ occupies 8*h* sites. It was noted that compounds containing only Sr^{2+} show longer Sr(1)-O and Sr(1)-F bond distances than those usually associated with 10-coordinate Sr^{2+} cations. Bond valence sum calculations for the $Sr^{2+}(1)$ site of $Sr_{3-x}A_xMO_4F$ (where A = Ca^{2+}, Ba^{2+}, and Sr^{2+} and M = Al^{3+} and Ga^{3+}) yielded a significantly lower figure when compared to the expected value. Substitution with the larger iso-valent Ba^{2+} cation (when compared to Sr^{2+}) enhances the bond valence sum for this site. Partial replacement of $Sr^{2+}(1)$ with Ba^{2+} could stabilize the structure due to the larger size of 10-coordinated Ba^{2+} cations ($r = 1.52$ Å) occupying the site more effectively than 10-coordinate Sr^{2+} cations ($r = 1.36$ Å). It has been reported that Ba^{2+} cations can be easily incorporated at the $Sr^{2+}(1)$ sites, while smaller Ca^{2+} cations ($r = 1.12$ Å) predominantly occupy $Sr^{2+}(2)$ sites, which have a smaller cationic radius and are more compatible with the sites occupied by 8-coordinate Sr^{2+} ($r = 1.26$ Å). These materials, however, are slightly moisture-sensitive, which is a common feature of oxyfluorides, but are relatively stable and can be processed for a few hours without taking any precautions. Overall, this structure is robust and can support bonding on $Sr^{2+}(1)$ and $Sr^{2+}(2)$ sites. Niyang et al. performed first-principles calculations on the $4f \rightarrow 5d$ transitions of Ce^{3+} located at the 10-coordinate $Sr^{2+}(1)$ and 8-coordinate $Sr^{2+}(2)$ sites of SAF, with local charge compensation by nearby Na'_{Sr} or coordinating O'_F substitution, to better understand the optical properties of the material. The supercell model was first employed to optimize the local structures of Ce^{3+}, based on which Ce-centered embedded clusters were constructed and wave function-based calculations with spin-orbit coupling were carried out to evaluate the energies of Ce^{3+} $4f^1$ and $5d^1$ levels. It was found that the incorporation of charge-compensated Ce^{3+} into SAF causes an anisotropic distortion of its local structure, which is especially pronounced in the case of compensation with a coordinating O'_F. Supercell total-energy calculation revealed that the dopant Ce^{3+} prefers to occupy smaller $Sr^{2+}(2)$ sites larger $Sr^{2+}(1)$ sites while following a similar charge-compensation mechanism.

In LSA (Figure 2c) structure model derived from the structural explanation of tetragonal $EuSr_2AlO_5$ reported by Drofenik and Golic. This structure contains slabs of $Sr^{2+}(2)$ and isolated $Al(O2)_4$ tetrahedra alternating with slabs of O(1) and (La/Sr(1)). $Sr^{2+}(2)$ has 10 coordination sites with respect to O(2) and O(1). La and $Sr^{2+}(1)$ occupy the distorted 8*h* site with approximately 8 coordination locations. The geometry of this site is depicted alongside the unit cell description. Im et al.[36] analyzed the local structure of LSA using pair distribution function (PDF) analysis, which showed that that despite their occupying the same crystallographic site, La and Sr have distinct coordination environments; the environment around La is more compact and regular than the environment obtained after the Rietveld refinement of the average structure as shown in Figures 3a–3e. It is also further confirmed by the maximum entropy method (MEM) analysis and it can be seen that the MEM electron density around this site is clearly nonspherical, unlike what is observed around all other sites in the unit cell as shown in Figures 3f and 3g. The curious bi-lobed shape of the electron density around the 8*h* site suggests the possibility of distinct coordination of La and Sr1 on this site as shown in Figure 3h.

Overall, the unit cell of SAF, and LSA the AlO_4 tetrahedra have strictly parallel upper and lower edges, which are parallel to the face diagonal of the (001) plane, while the SiO_4 tetrahedra in SSO rotate relative the each other, which leads to a lower symmetry for the space group *P4/nnc* as compared to the space group *I4/mcm*. Due to such structural compatibility, various combinations of continuous binary solid-solutions can be formed with SAF, LSA, and SSO host compounds.

Strategy-2: Modification of Chemical Composition by Cation or Anion Substitution

In this section, we discuss the optical properties of rare-earth-activated SSO, SAF, and LSA phosphors and then analyze the influence of co-dopants on the luminescence properties of these materials.

Jang et al.[37,38] prepared Ce^{3+}-activated SSO phosphor via solid-state synthesis with Li^+ co-doping, which helps to introduce Ce^{3+} ions into Sr^{2+} sites by charge compensation. Figure 4a shows the photoluminescence excitation (PLE) and photoluminescence (PL) spectra of SSO:Ce^{3+}, Li^+. The excitation band exhibits broad absorption ranging from 200 to 500 nm and intense yellow emission at ~532 nm. Additionally, the emission wavelength of SSO:Ce^{3+}, Li^+ can be adjusted by changing the amount of Ce^{3+} and color temperature (T_c). In addition, the CRI of SSO:Ce^{3+}, Li^+-based WLEDs can be controlled without mixing different kinds of phosphors. Luo et al. found that the emission spectrum of this phosphor can also be tuned by changing the crystal field of Ce^{3+} by substituting Si^{4+} with Al^{3+}, Ga^{3+}, and B^{3+}[39]. At the same time, PL intensity improved due to the compensation of charge imbalance between Ce^{3+} and Sr^{2+}. Zhu et al.[40] prepared Mg^{2+} and Ba^{2+} co-doped SSO:Ce^{3+}, Li^+ phosphors. When they replaced Sr^{2+} ions with smaller Mg^{2+} ions, the emission wavelength shifted from 532 to 517 nm. On the contrary, when Sr^{2+} ions were partially replaced by larger Ba^{2+} ions, the emission wavelength shifted to higher wavelengths from 532 to 552 nm. This phenomenon can be explained in terms of an increase or decrease in the nephelauxetic effect. Upon replacing Sr^{2+} ions with Mg^{2+} ions, the degree of covalency in Ce-O decreased, resulting in a blue-shift in the emission band. In a similar manner, the introduction of Ba^{2+} ions at Sr^{2+} sites led to an increase in the degree of covalency of Ce-O, which results in the emission band shifting to higher wavelengths. Generally, phosphors crystallized using highly symmetrical compounds exhibit high luminescence efficiency. These phosphor materials exhibit a reduction in PL intensity with the introduction of Ba^{2+} and Mg^{2+} ions at Sr^{2+} sites as they experience a reduction in symmetry.[41]

Green et al.[35,42] reported that the self-activated PL properties of SAF at a 254 nm excitation wavelength include a broad bluish-white emission. They found that the existence of two distinct clusters is

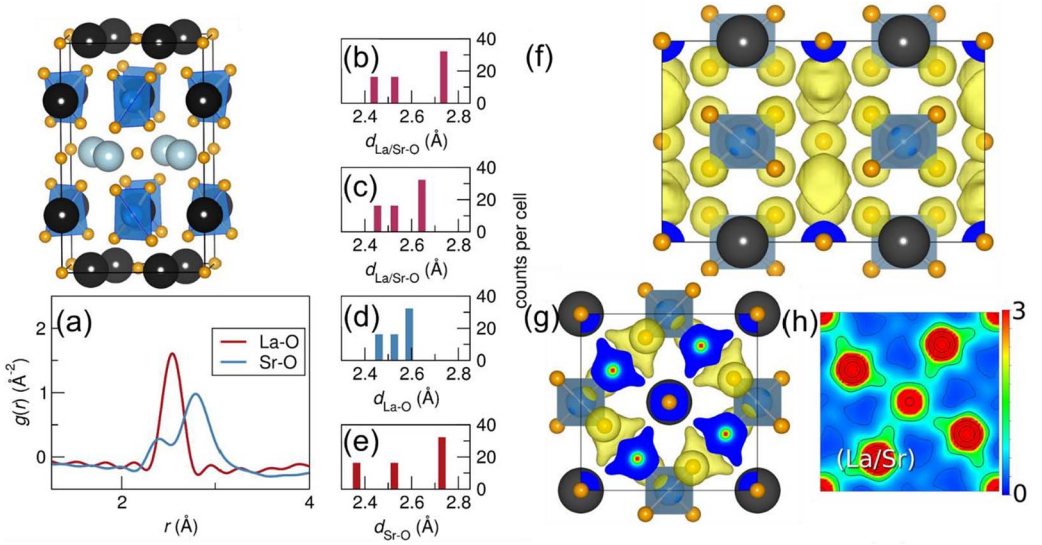

Figure 3. The local structure model of LSA:Ce^{3+}, featuring layers of Sr1 (large light gray spheres) and La/Ce (large dark spheres) stacked along [001], and depicted with refined parameters from the 20 Å PDF fit. The model can be indexed in the *P*4/*mbm* space group (No. 127) with La/Ce at 4h (x, x + 0.5, 0.5), Sr1 at 4g (x, x + 0.5, 0), Sr2 at 4*e* (0, 0, z), Al at 4*f* (0, 0.5, z), O1 at 2*a* (0, 0, 0), O2 at 2*b* (0, 0, 0.5), O3 at 8*k* (x, x + 0.5, z); and O4 at 8*k* (x, x + 0.5, z). O layers above and below the La layer (O4 positions) give rise to smaller and more regular distorted octahedra around La atoms. Note the elongation of the AlO_4 tetrahedra. (a) The partial pair correlation functions for La–O and Sr1-O extracted from the local structure fit. (b–e) Respective distribution of (La/Sr1)-O distances resulting from (b) the *I*4/mcm Rietveld refinement parameters, (c) the *I*4/*mcm* PDF refinement parameters, and (d–e) the local structure *P*4/mbm PDF model refinement parameters which yield separate La–O and Sr1-O distances 1 $Å^{-3}$ MEM isosurface of the electron density depicted within the unit cell of LSA. (f) depicts a projection down the axis of the unit cell, and (g) depicts a projection down the c axis, showing the plane containing the 8*h* site with (La/Sr1) with O1 at the center and corners. The non-spherical nature of the electron density around the 8h site is evident. (h) displays the (001) plane of the structure showing a map of the MEM electron density. The scale bar for coloring of the map is depicted alongside, as a percentage of the strongest peaks in the MEM electron density (Reprinted with permission from Ref. 28 Jounal of Material Chemistry).

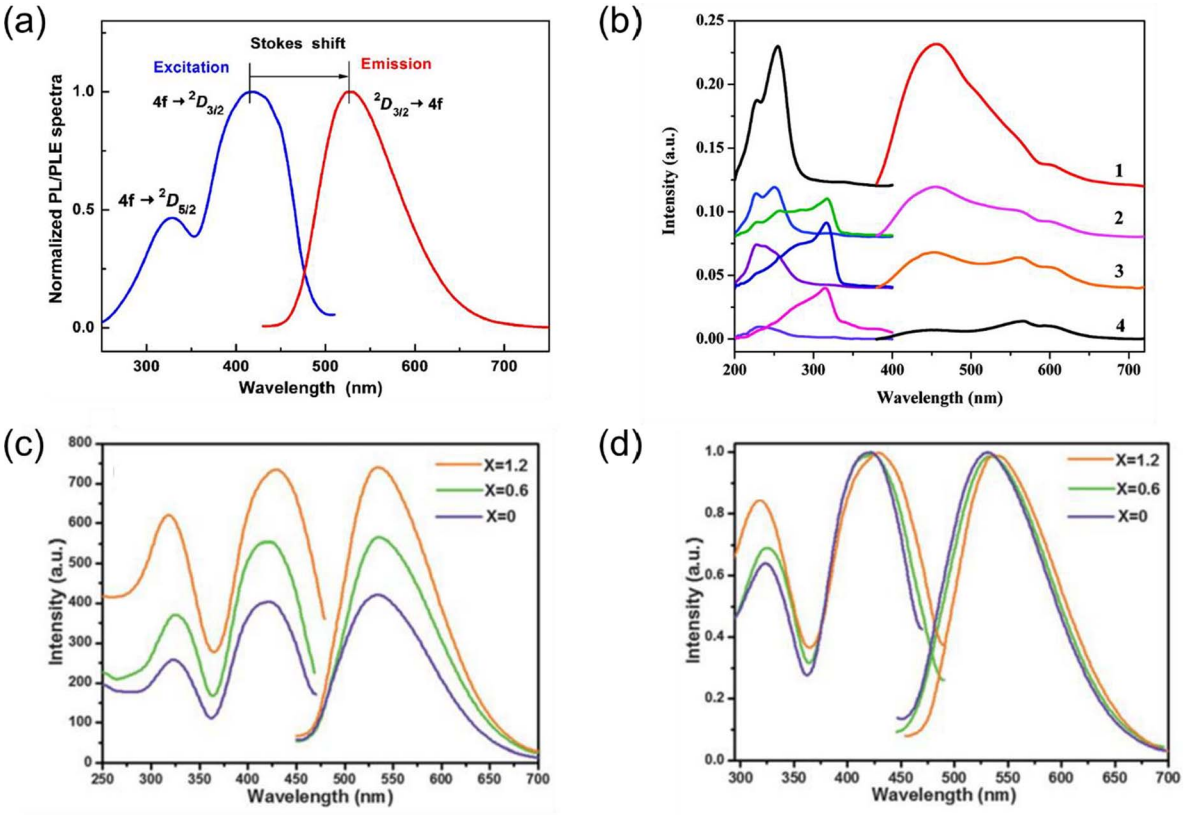

Figure 4. (a) Represents the excitation and emission spectra of SSO:Li^+,Ce^{3+} phosphor (Reprinted with permission from Ref. 29. Copyright Applied Physics Letter.) (b) PL spectra of the $Sr_{2.4}Ba_{0.6}AlO_4$-$RF_{1-\delta}$ phosphors. The numbers indicate the reducing gas flow rates (Reprinted with permission from Ref. 34. Copyright Journal of Physical Chemistry C). (c) PL spectra of $Sr_{2.97-x}$ $Ca_xCe_{0.02}Al_{0.2}Mg_{0.4}Si_{0.4}O_4F$ with varying Ca^{2+} concentration. (d) Position of the excitation and emission maximum after being normalized (Reprinted with permission from Ref. 41. Copyright Journal of Material Chemistry C).

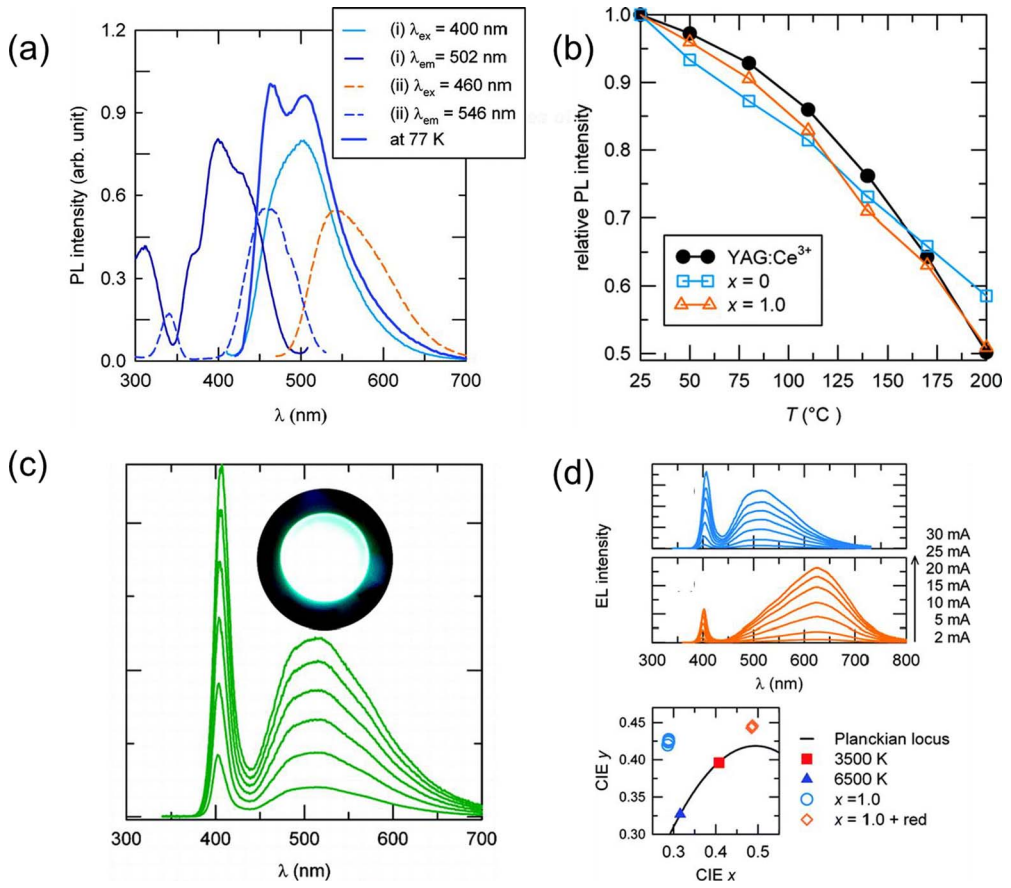

Figure 5. (a) Excitation and emission spectra of (i) SBAF:Ce^{3+} at room temperature compared with a (ii) commercial YAG:Ce^{3+}phosphor. The PL emission spectra of SBAF:Ce^{3+} at 77 K is also displayed. (b) PL intensities for thermal quenching of commercial YAG:Ce^{3+}, SBAF (x = 0), and SBAF (x = 1.0)in the temperature range from 25 to 200°C. (c)&(d) represents the luminescence of the InGaN LED phosphor, under different forward bias currents (indicated): and CIE chromaticity coordinates of the device under different forward bias currents (Reprinted with permission from Ref. 42. Copyright Chemistry of Materials).

responsible for this self-activating PL. Moreover, they noticed that when the flow of reducing gas was varied from lb/1s to lb/5s, the emission color of this material changed from bluish-white to yellow with the substitution of Ba^{2+} ions at Sr^{2+} sites (Figure 4b). This behavior indicates the presence of various defect clusters within the material that may be held responsible for the differences in PL properties.

Fang et al.[43] reported SAF:Na^{+}, Ce^{3+} phosphors that exhibit a broad blue-green emission at 506 nm when excited at 405 nm. Upon varying the excitation energy, the shape of the emission spectra did not change but the emission wavelength of Ce^{3+} shifted to longer wavelengths. This phenomenon can be attributed to the occupation of different Sr^{2+} sites by Ce^{3+}. In addition, they also calculated the energy level of $[Ce(1)O_8F_2]^{-15}$ and $[Ce(2)O_6F_2]^{-11}$ clusters by the DV-Xα method.[44–46] This calculation showed that the presence of mixed bonding of O/F in this phosphor plays an important role in stabilizing Ce^{3+} ions at $Sr(1)^{2+}$ sites. Moreover, Shang et al.[47] studied the energy transfer between (Eu^{3+}, Tb^{3+}) and (Ce^{3+}, Tb^{3+}) ions. They observed that for SAF:Ce^{3+}, Tb^{3+} samples, energy transfer from Ce^{3+} to Tb^{3+} is efficient and confirmed resonance via dipole-quadrupole interactions using experimental and theoretical calculations. Meanwhile, Noh et al.[48] tuned the emission color from blue to orange-red by activating with Bi^{3+} and Eu^{3+} ions; they claimed that the color tunable emission is a result of Bi^{3+} and Eu^{3+} transitions in cooperation with blue and red activators in the host lattice and not because of energy transfer between Bi^{3+} and Eu^{3+} ions.

In addition, Zheng et al.[49] tuned the structural and optical properties of SAF:Ce^{3+} phosphors by substituting Mg^{2+}-Si^{4+} for Al^{3+} pairs and Ca^{2+} for Sr^{2+}. An increase in the concentration of Mg^{2+}-Si^{4+} at Al^{3+} sites enhanced the intensity; further, a yellow emission was observed along with a gradual red-shift in both the excitation and emission spectra Figures 4c and 4d. Here, two processes contributed to the red-shift. The first one is the compression of polyhedral 8-coordinate $Ce(2)^{3+}$ by substituting Mg^{2+}-Si^{4+} for Al^{3+} pairs and limiting the occupancy of $Ce(1)^{3+}$ by the replacement of Sr^{2+} with Ca^{2+} ions.

Im et al.[36,50] reported that LSA:Ce^{3+} phosphors showed a broad yellow emission (556 nm) when excited at 450 nm. The same research group extensively studied the optical properties of these compounds by co-doping them with different elements. Firstly, two substitutions with anions (F^{-} for O^{2-}) and cations (Ba^{2+} for Sr^{2+}) resulted in the oxyfluoride phosphor family of $Sr_{2.975-x}$ $Ba_xCe_{0.025}AlO_4F$ (SBAF:Ce^{3+}) and 100% PLQY[51] due to an increase in electron–phonon coupling after the introduction of F at O sites. This phosphor exhibits emission maxima at 502 nm (Figure 5a) when excited at 405 nm; further, its temperature-dependent PL properties exhibit high thermal stability when compared to those of commercial YAG:Ce^{3+} phosphors as depicted in Figure 5b. When SBAF:Ce^{3+} was incorporated with an encapsulant in a UV-LED, a greenish-white light with a CRI of 62 was observed under a forward-bias current of 20 mA as shown in Figures 5c and 5d. Secondly, the researchers studied the substitution of Gd^{3+} for La^{3+}, Ca^{2+}, Ba^{2+} for Sr^{2+}, and B^{3+} or Ga^{3+} for Al^{3+}. All the above cation substitutions/solid-solution are attained to the full extent except when Ca^{2+} (for Sr^{2+}) or B^{3+} (for Al^{3+}). The luminescence properties of the prepared Ce^{3+} phosphors were dependent on rare-earth metal-oxygen distances and lattice ionicity. LSA:Ce^{3+}-based phosphor compositions feature a wide range of emission peak wavelengths (545–577 nm) as a result of a decrease in the Ce-O average bond length. Furthermore, Yu et al. studied the optical properties of LSA:Ce^{3+} phosphors by controlling the chemical composition ratio between La^{3+} and Gd^{3+}. They found that with an increase in the Gd^{3+}/La^{3+} ratio, the PL spectra red-shifted and this behavior can be

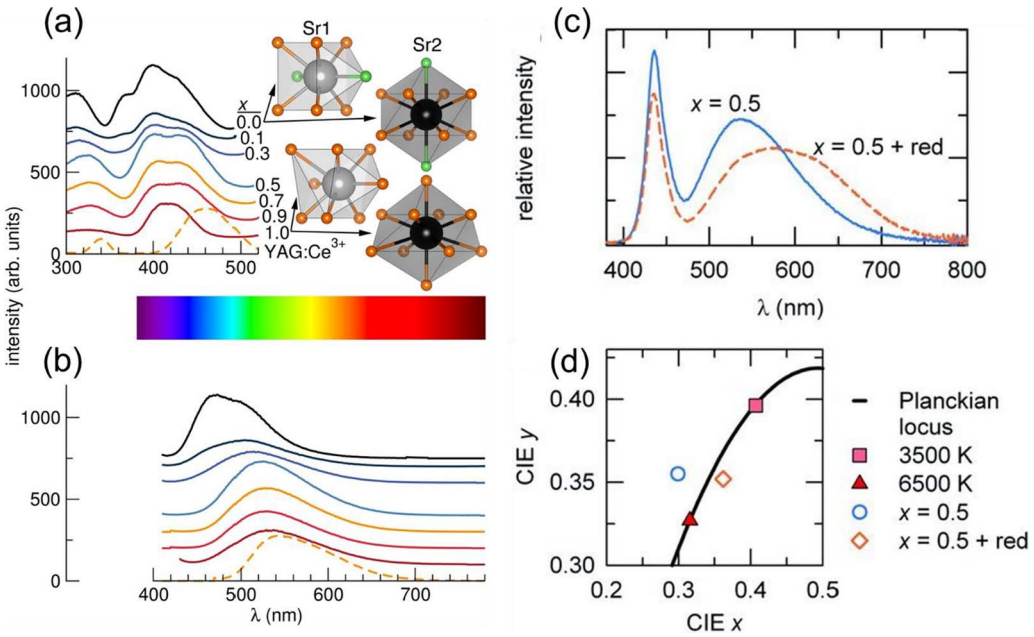

Figure 6. (a) Excitation and (b) emission spectra of the solid solution phosphors SASF:$Ce^{3+}$with the various x values indicated. For comparison, the excitation and emission spectra of a YAG:Ce^{3+} phosphor are also shown. Spectra have been offset for clarity. Sr1 and Sr2 polyhedra looking down the [100] direction are shown to the right of (a); the upper two polyhedra are from the SAF structure and the lower two are from the SSO structure. Light gray, black, orange, and green spheres represent Sr1, Sr2, O, and F atoms, respectively. (c) Electroluminescence spectra of the SASF phosphor ($x = 0.5$) with (dashed) and without (solid) a red phosphor incorporated into an InGaN LED ($\lambda_{max} = 434$ nm) under 20 mA forward bias current and b) CIE chromaticity coordinates of the device. The Planckian locus line and the points corresponding to color temperatures of 3500 K and 6500 K are indicated in (d) (Reprinted with permission from Ref. 44. Copyright Advanced Materials).

attributed to an enhanced covalence. The emission intensities initially increased but decreased later; the maximum intensity was obtained at of 60%Gd^{3+} substitution in La^{3+} sites.

Strategy-3: Modification of Chemical Composition by Chemical Unit Co-Substitution

In recent times, solid-solution phosphors have attracted much research attention. Especially, oxyfluoride phosphors with a wide range of luminescence properties are being developed; such wide ranges can be attributed to the evolution of their compositions and crystal structures. In this section, we emphasize the tunability of optical properties by forming a solid-solution with Ce^{3+}-activated SAF, LSA, and SSO phosphor materials.

Im et al.[52] developed a green-yellow emitting phosphor by forming a solid-solution between Ce^{3+}-activated SSO and SAF (forming SSAF:Ce^{3+}) with a high PLQY of ~85%. With an increase in the SSO content, both the excitation and emission spectra shifted monotonically to longer wavelengths (Figures 6a and 6b). This phenomenon may be attributed to an increase in distortion around the active sites and increasing covalency. Further, they adopted a phosphor-capped layer with an air gap between the epoxy layer on the LED chip gives the white light with an efficacy of 73 lm/W under 20 mA forward as shown in Figures 6c and 6d. Lee et al.[53] demonstrated the energy-transfer mechanism in Tb^{3+} co-activated phosphors in SSAF:Ce^{3+}. The mechanism was identified to be electric dipole–quadrupole interaction by decay analysis using the Inokuti-Hirayama model. In addition, Im et al. reported two combinations of solid- solutions of two isotopic compounds from the end members LSA and SSO (forming LSAO); further, $GdSr_2AlO_5$ (GSA) and SAF (forming GSAF)[54] act as hosts for Ce^{3+} activator ions.[55] In the case of LSAO:Ce^{3+} phosphors, their PL intensity depends on the excitation wavelength. The highest PL intensities were obtained at 90% co-substitution of SSO. By careful examination of the structural properties of these two host materials in LSAO, the researchers found that there occurred compositional disordering at La^{3+}/Sr^{2+} sites, which altered the Ce^{3+} crystallographic environment and thus enhanced the PL intensity. They obtained a white light with a color rendering index (Ra) between 67 and 70 and color temperatures between 6550 and 7345 K with relatively high efficacies. However, the GSAF:Ce^{3+} phosphor exhibited a reduced PL intensity, which may be attributed to the decreased crystal field splitting arising from increased host ionicity with fluorine addition. Kristin et al.[56] reported the inclusion of a Ce^{3+}-activated solid-solution phosphor in between SBAF and SSO. They tuned the emission wavelength of the phosphor from 523 to 553 nm by tuning its chemical composition as shown in Figures 7a and 7b. This phenomenon is attributed to an increase in distortion around the active sites and increased covalency, which resulted in a red-shift in the emission spectra. The maximum emission wavelength of these phosphors could be tuned from green to yellow by tuning their composition (Figure 7c) and a high PLQY of 70% could be achieved. To further demonstrate the potential application of this series of Ce^{3+}doped (1-x)SSO-xSBAOF phosphors, combined three typical phosphor samples into one component,using the red component, with a bluish violet InGaN LED chip to realize white light as shown in Figure 7d. Recently, Unithrattil et al.[57] reported a series of ternary solid-solution phosphors based on three end members with similar structures and slightly different space groups for SSO, SAF, and LSA. Surprisingly, ternary solid-solutions of the vertex members SSO, SAF, and LSO form single-phase compounds (Figure 8a). The investigators found that compounds near the centroid have a greater ability to withstand lattice strain arising from the distortion of polyhedral alignment in the solid-solution. Moreover, it was realized that emission from the compound with a 1:2:1 ratio of the end members was the most intense (Figure 8b). The PL spectra of a selected compound AB_2C were studied at various activator concentrations Figure 8c. The compound showed approximately similar emission intensities for a wide range of activator concentrations ranging from 0.05 to 0.30 mol and the highest PL intensity was obtained at a doping concentration of 0.025 mol. Moreover, the temperature dependence of the PL properties of AB_2C:Ce^{3+} phosphors was found to decrease with an increase in temperature and was nearly identical at different activator concentrations. Figure 8d shows the relative PL intensity was

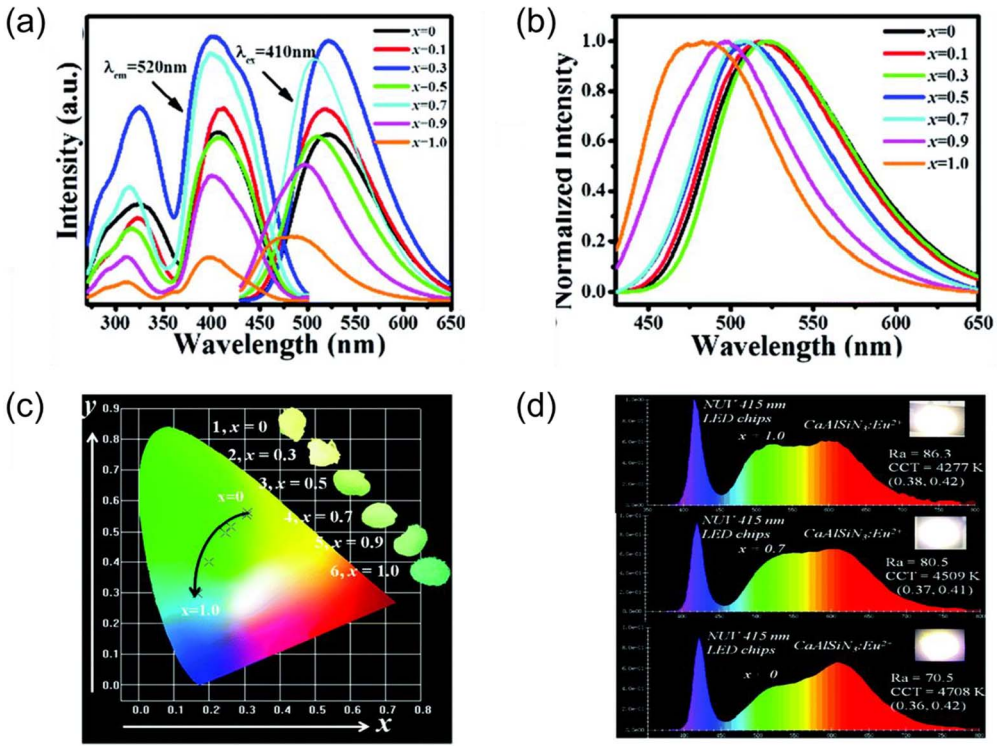

Figure 7. (a) The PLE and PL spectra of (1-x)SSO-xSBAOF:Ce^{3+}solid-phosphor. (b) Normalized PL spectra of (1-x)SSO-xSBAOF:Ce^{3+}solid-phosphor. (c) CIE chromaticity diagram for a series of (1-x)SSO-xSBAOF. (d) The electroluminescence spectra of (1-x)SSO-xSBAOF:Ce^{3+}solid-phosphor, synthesized using the two-step method, under a forward bias current of 30 mA. The inset images show the illumination of the LED lamp, excited at 365 nm. Inset images: digital photographs of these phosphors (Reprinted with permission from Ref. 48. Copyright Journal of Material Chemistry C).

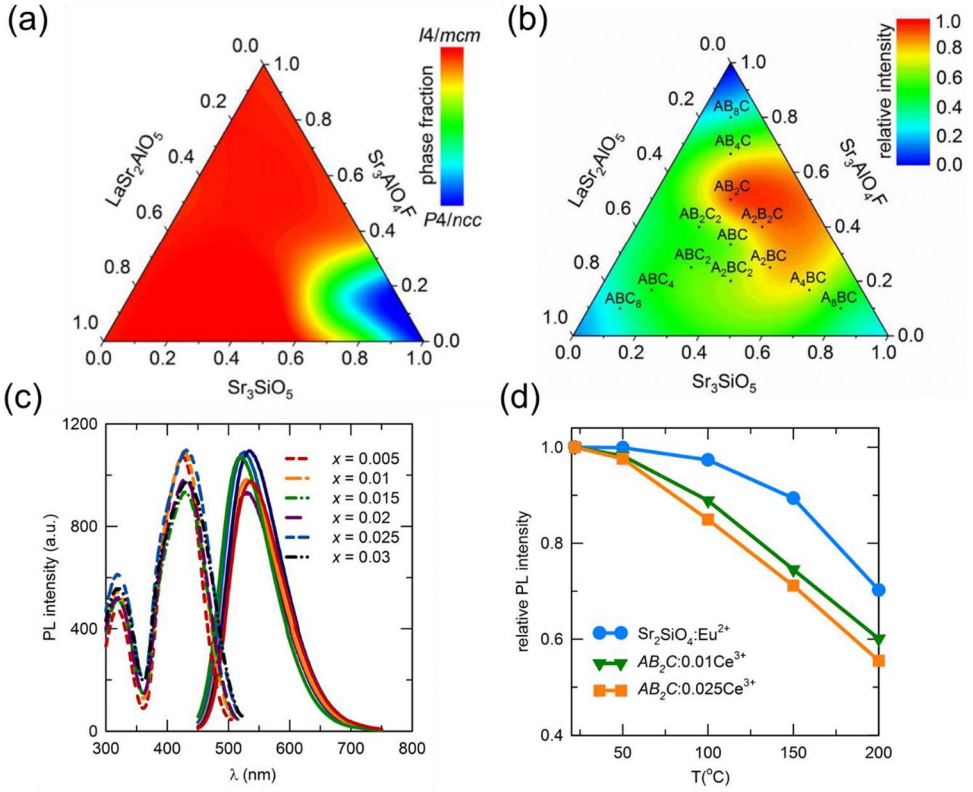

Figure 8. (a) The ternary contour diagram representing the prominent phase of solid-solution compounds. (b) Ternary contour diagram illustrating the relative intensity of host compositions on activation with Ce^{3+}ions. The compound represented by $AB_2C:Ce^{3+}$ has the highest emission intensity. (c) PLE and PL of $AB_2C:Ce^{3+}$ for different activator concentrations. (d) Temperature dependence of emission intensity in comparison with $Sr_2SiO_4:Eu^{2+}$(Reprinted with permission from Ref. 50. Copyright Journal of alloys and compounds).

Table I. Summary of oxy-fluoride phosphor excitation and emission wavelengths, CIE coordinates and PLQY values respectively.

phosphor	excitation maxima λ_{max} (nm)	emission maxima λ_{max} (nm)	CIE coordinates	PLQY(%)
$Sr_{2.4}Ca_{0.45}Tb_{0.1}AlO_4F$	270 nm	550 nm	$x = 0.30$, $y = 0.52$ ($\lambda_{ex} = 270$ nm)	-
$Sr_{2.4}Ba_{0.45}Tb_{0.1}AlO_4F$	270 nm	550 nm	$x = 0.27$, $y = 0.44$ ($\lambda_{ex} = 270$ nm)	-
$Sr_{2.85}Tb_{0.1}AlO_4F$	270 nm	550 nm	$x = 0.31$, $y = 0.53$ ($\lambda_{ex} = 270$ nm)	-
$Sr_{2.85}Tb_{0.1}Al_{0.5}Ga_{0.5}O_4F$	265 nm	550 nm	$x = 0.30$, $y = 0.52$ ($\lambda_{ex} = 265$ nm)	-
$Sr_{2.8}Ca_{0.2}GaO_{4-}\alpha F_{1-\delta}$	254 nm	487 nm	$x = 0.25$, $y = 0.40$ ($\lambda_{ex} = 254$ nm)	-
$Sr_{2.8}Ba_{0.2}GaO_{4-}\alpha F_{1-\delta}$	254 nm	483 nm	$x = 0.28$, $y = 0.46$ ($\lambda_{ex} = 254$ nm)	-
$Sr_3AlO_{4-}\alpha F_{1-\delta}$	254 nm	476 nm	$x = 0.21$, $y = 0.38$ ($\lambda_{ex} = 254$ nm)	-
$Sr_3GaO_{4-}\alpha F_{1-\delta}$	254 nm	476 nm	$x = 0.27$, $y = 0.43$ ($\lambda_{ex} = 254$ nm)	-
$Sr_{2.25}Ba_{0.6}Eu_{0.1}Al_{0.95}In_{0.05}O_{4-}\alpha F_{1-\delta}$	300 nm	615 nm	$x = 0.49$, $y = 0.50$ ($\lambda_{ex} = 300$ nm)	-
$Sr_{2.25}Ba_{0.6}Eu_{0.1}Ga_{0.95}In_{0.05}O_{4-}\alpha F_{1-}\delta$	300 nm	620 nm	$x = 0.50$, $y = 0.49$ ($\lambda_{ex} = 300$ nm)	-
$Sr_{2.4}Ba_{0.6}Al_{0.9}In_{0.1}O_{4-}\alpha F_{1-}\delta$	365-372	580 nm	$x = 0.58$, $y = 0.42$	-
$Sr_{2.85}Eu_{0.1}Al_{0.9}In_{0.1}O_{4-}\alpha F_{1-}\delta$	365 nm	580 nm	$x = 0.57$. $y = 0.42$ ($\lambda_{ex} = 365$ nm)	-
$Sr_3AlO_{4-}\alpha F_{1-}\delta$ (700°C, 1b/1s)	254 nm	585 nm	$x = 0.20$, $y = 0.26$ ($\lambda_{ex} = 254$ nm)	-
$Sr_3AlO_{4-}\alpha F_{1-}\delta$ (900°C, 1b/1s)	254 nm	480 nm	$x = 0.26$, $y = 0.34$ ($\lambda_{ex} = 254$ nm)	-
$Sr_3AlO_{4-}\alpha F_{1-}\delta$ (900°C, 1b/4s)	254 nm	585 nm	$x = 0.22$, $y = 0.41$ ($\lambda_{ex} = 254$ nm)	-
$Sr_3AlO_{4-}\alpha F_{1-}\delta$ (entire synthesis in $5\%H_{2(g)}/95\%Ar_{(g)}$)	254 nm	578 nm	$x = 0.23$, $y = 0.55$ ($\lambda_{ex} = 254$ nm)	-
$Sr_{2.5}Ca_{0.5}Al_{0.9}In_{0.1}O_{4-}\alpha F_{1-}\delta$	365 nm	576	$x = 0.46$, $y = 0.51$ ($\lambda_{ex} = 365$ nm)	-
$Sr_{2.5}Ba_{0.5}Al_{0.9}In_{0.1}O_{4-}\alpha F_{1-}\delta$	365 nm	599	$x = 0.55$, $y = 0.44$ ($\lambda_{ex} = 365$ nm)	-
$Sr_{2.975}Ce_{0.025}AlO_4F$	420 nm	460	–	83%
$Sr_{1.975}BaCe_{0.025}AlO_4F$	420 nm	502	–	95%
$2Sr_{3-2x}Ce_xNa_xAlO_4F$ ($x = 0.03$)	310, 405	458, 500, 531, 593	–	-
$Gd_{1-x}Sr_{2+x}AlO_{5-x}F_x:Ce^{3+}$ ($x = 0$)	403	574	–	-
$Gd_{1-x}Sr_{2+x}AlO_{5-x}F_x:Ce^{3+}$ ($x = 1$)	453	474	–	-
$Sr_{2.975}Ce_{0.025}Al_{1-x}Si_xO_{4+x}F_{1-x}(x = 0)$	420 nm	474	–	-
$Sr_{2.975}Ce_{0.025}Al_{1-}xSi_xO_{4+x}F_{1-}x(x = 1)$	420 nm	537	–	85%
$Sr_{2.425}Ba_{0.5}Sm_{0.05}AlO_4F$	240	565, 604, 644, 707 ($\lambda_{ex} = 254$, 408 nm)	–	-

analyzed at various temperatures ranging from 25 to 200°C and the activation energy for thermal quenching was determined as 0.316 eV and 0.303 eV at activator concentrations of 0.01 and 0.025 mol, respectively.

A summary of the reported Cs_3CoCl_5 family members and their luminescent properties is included in Table I. This is anticipated to be a simple literature synopsis rather than a quantitative comparison.

Perspective and Summary

In this review, we systematically explained the structural and optical properties of isostructural hosts belonging to or closely related to the Cs_3CoCl_5 family. The excellent optical properties of these broadband emission phosphors is attributed to the flexible crystallographic environment of their cations due to either chemical substitution of co-dopants or replacement of the chemical unit. The high PLQY and low thermal quenching properties of these oxyfluoride compounds may be attributed to the soft phonon modes associated with F atoms in the host crystal. However, our analysis of these materials indicates that there exists a strong correlation between the PLQY, E_g, location of the activation center, local coordination around the activation center, and the calculated Debye temperature of the host crystal structure. This correlation allows us to rapidly screen many potential phosphor hosts for WLED applications and ultimately, it will assist in the discovery of next-generation WLEDs.

One feasible method for identifying materials with a high PLQY is to find structurally rigid host materials with high atomic connectivity. These characteristics enhance their PLQY by constraining soft phonon modes that lead to non-radiative relaxation, thereby increasing their tendency for photon emission. However, the complex nature of chemical bonding in inorganic solids makes it challenging to clearly identify their connectivity and structural rigidity. Therefore, material scientists are employing the technique of machine learning, which can rapidly analyze any given combination of elements, stoichiometry, or unit cells. However, the major challenge in this approach lies in determining the effectiveness of the algorithms. Data based on different algorithms should be processed before being provided as input to other algorithms.

Although highly connected structures with a large Debye temperature can yield potential phosphor hosts, that is not sufficient to produce an excellent phosphor. The E_g is also an essential material parameter that should be considered; it should be large enough to accommodate electronic transitions of the rare-earth luminescent center. However, a large Debye temperature arising from highly connected structures and a wide E_g are often contraindicatory. Following band dispersion arguments, increased atomic interactions (bonds) lead to greater dispersion of band structures, often resulting in a narrow E_g. Thus, the connectivity in any potential host must be carefully balanced with the E_g to ensure sufficient photoluminescence. These two parameters can be optimized by plotting Debye temperature as a function of the calculated E_g, which serves as a sorting diagram, as shown in Figure 9.[58,59] Moreover, we explained the processing steps in order to use the machine learning programme: (1) Employ the data-mined ionic substitution algorithm to identify the viable candidates of phosphor host materials. (2) Check the evaluated compounds whether existed in the data bases like international crystallographic data base (ICSD). (3) Calculate the crystal rigidity using quasi harmonic Debye model. (4) Employ the Perdew-Burke-Ernzerhof (PBE) functional model to calculate the E_g of the materials. (5) Finally, plot the diagram E_g Vs. Debye temperature which illustrates the potential host for LED applications. There is not much information on the discovery of new inorganic phosphors based on fluorine-containing materials using machine learning techniques. Here, we propose that co-substitution of N in the

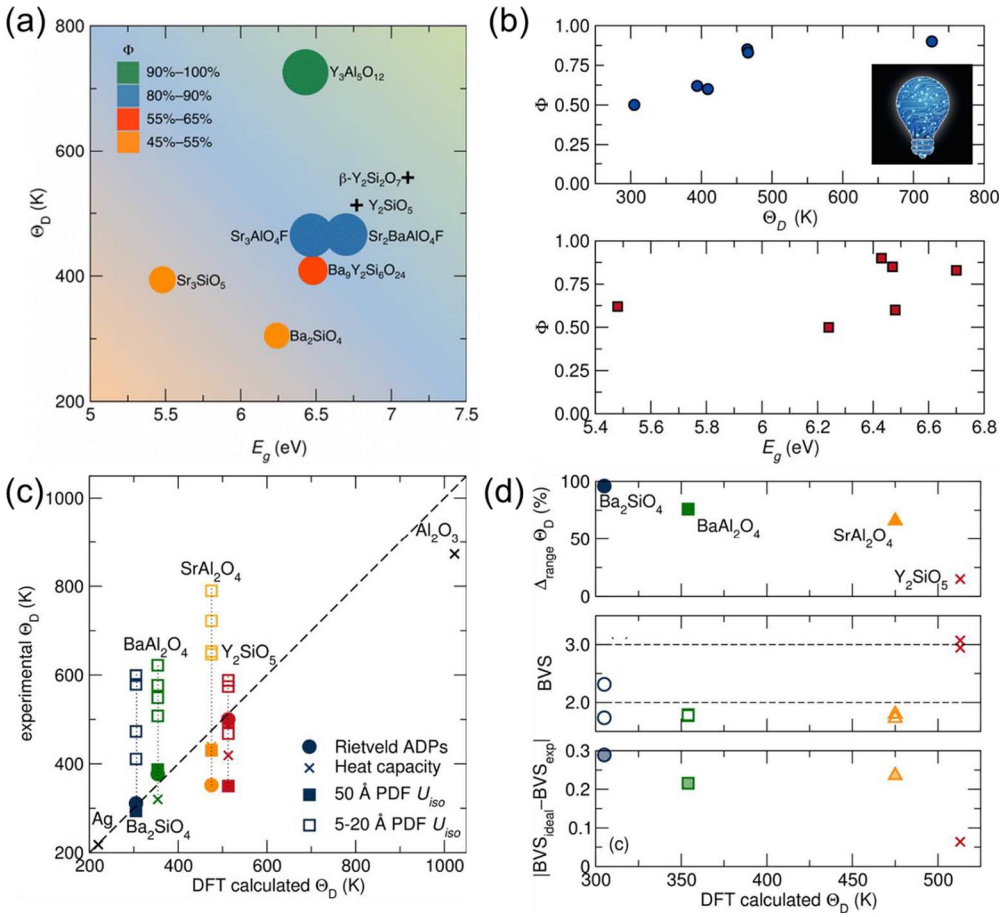

Figure 9. (a) A plot of the calculated Debye temperature as a function of calculated E_g calculated using the HSE06 functional, for the different compounds considered here. The circle size and color are indicative of the experimentally measured PLQY when Ce^{3+} is incorporated. (b) The experimentally measured PLQY versus the (a) calculated Debye temperature and the (b) calculated E_g using the HSE06 hybrid functional (Reprinted with permission from Ref. 51. Copyright Journal of Physical Chemistry C). (c) Calculated Debye Temperature from DFT and experimental Debye Temperature determined using atomic displacement parameters from Rietveld and PDF refinements of low-temperature neutron powder diffraction data collected at 15 K and extracted from low-temperature heat capacity collected at 1.8 K for all compositions. The different data points for the PDF refinements indicate increasing values of r_{max}, with the trend that the PDF-calculated Debye temperature for each sample decreases with increasing r_{max}. Also included as a reference are the Debye Temperature for silver and alumina measured using the low-temperature heat capacity method. (d) Difference in measured Debye Temperature from the local structure 1–5 Å PDF fitting range and the average structure DFT calculated Debye Temperature as a percentage of the expected DFT calculated Debye Temperature, the bond valence sums (BVSs) for each cation site in each composition determined from Rietveld refinement of neutron diffraction data collected at 15 K showing the deviation from ideal 2+ for Ba^{2+} and Sr^{2+} and ideal 3+ for Y^{3+}, and the average deviation from ideal bond valence sums weighted by site multiplicity shows that for more optimized structures the changes in measured Debye Temperature as a function of PDF fitting range and the difference in bond valence sum from ideal is smaller, coinciding with higher Debye Temperature materials Reprinted with permission from Ref. 50. Copyright ACS Applied Materials Interfaces).

Ce^{3+}-activated Cs_3CoCl_5 family can result in suitable luminescence properties due to their appropriate structural characteristics. Therefore, research on photoluminescent materials based on fluorine-containing materials should be continued intensively to rapidly develop solid-state lighting technology.

Acknowledgments

This research was supported by the Basic Science Research Program through National Research Foundation of Korea (NRF), funded by the Ministry of Science, ICT & Future Planning (Project no. 2017R1A2B3011967). This research was supported by Global Ph.D. Fellowship Program through the NRF funded by Ministry of Education (NRF-2018H1A2A1062877). This work was supported by the Engineering Research Center through National Research Foundation of Korea (NRF), funded by the Korean Government (MSIT), (Project No. NRF-2018R1A5A1025224). This work was also supported by the Technology Innovation Program (KEIT-20002947) funded by the Ministry of Trade, Industry & Energy (MOTIE, Korea). The manuscript was written through contributions of all authors. All authors have given approval to the final version of the manuscript.

ORCID

Won Bin Im https://orcid.org/0000-0003-2473-4714

References

1. E. F. Schubert, J. K. Kim, H. Luo, and J. Xi, Solid-state lighting—a benevolent technology. *Rep. Prog. Phys*, **69**(12), 3069 (2006).
2. K. A. Denault, J. Brgoch, M. W. Gaultois, A. Mikhailovsky, R. Petry, H. Winkler, S. P. DenBaars, and R. Seshadri, Consequences of Optimal Bond Valence on Structural Rigidity and Improved Luminescence Properties in $Sr_xBa_{2-x}SiO_4$: Eu^{2+} Orthosilicate Phosphors. *Chem. Mater.*, **26**(7), 2275 (2014).
3. K. Horky and W. Schnick, $Li_{24}Sr_{12}[Si_{24}N_{47}O]F$: $Eu^{2+}\square$ Structure and Luminescence of an Orange Phosphor. *Chem. Mater.*, **29**(10), 4590 (2017).
4. C. Maak, R. Niklaus, F. Friedrich, A. Mähringer, P. J. Schmidt, and W. Schnick, Efficient yellow-orange phosphor $Lu_4Ba_2[Si_9ON_{16}]O$: Eu^{2+} and orange-red emitting $Y_4Ba_2[Si_9ON_{16}]O$: Eu^{2+}: two oxonitridosilicate oxides with outstanding structural variety. *Chem. Mater.*, **29**(19), 8377 (2017).

5. E. Elzer, R. Niklaus, P. J. Strobel, V. Weiler, P. J. Schmidt, and W. Schnick, $MBe_{20}N_{14}$: Eu^{2+} (M = Sr, Ba): Highly Condensed Nitridoberyllates with Exceptional Highly Energetic Eu^{2+} Luminescence. *Chem. Mater.*, **31**(9), 3174 (2019).
6. Z. Wang, J. Ha, Y. H. Kim, W. B. Im, J. McKittrick, and S. P. Ong, Mining unexplored chemistries for phosphors for high-color-quality white-light-emitting diodes. *Joule*, **2**(5), 914 (2018).
7. G. J. Hoerder, M. Seibald, D. Baumann, T. Schröder, S. Peschke, P. C. Schmid, T. Tyborski, P. Pust, I. Stoll, and M. Bergler, Sr $[Li_2Al_2O_2N_2]$: Eu $^{2+}$-A high performance red phosphor to brighten the future. *Nat. Commun.*, **10**(1), 1824 (2019).
8. Y. Zhuo, A. M. Tehrani, A. O. Oliynyk, A. C. Duke, and J. Brgoch, Identifying an efficient, thermally robust inorganic phosphor host via machine learning. *Nat. Commun.*, **9**(1), 4377 (2018).
9. W. B. Park, S. P. Singh, and K.-S. Sohn, Discovery of a phosphor for light emitting diode applications and its structural determination, $Ba(Si,Al)_5(O,N)_8$: Eu^{2+}. *J. Am. Chem. Soc.*, **136**(6), 2363 (2014).
10. W. B. Park, N. Shin, K. P. Hong, M. Pyo, and K. S. Sohn, A New Paradigm for Materials Discovery: Heuristics-Assisted Combinatorial Chemistry Involving Parameterization of Material Novelty. *Adv. Funct. Mater.*, **22**(11), 2258 (2012).
11. W. B. Park, K. H. Son, S. P. Singh, and K.-S. Sohn, Solid-State Combinatorial Screening of $ARSi_4N_7$: Eu^{2+} (A = Sr, Ba, Ca; R = Y, La, Lu) Phosphors. *ACS Comb. Sci.*, **14**(10), 537 (2012).
12. Y. L. Tung, L. S. Chen, Y. Chi, P. T. Chou, Y. M. Cheng, E. Y. Li, G. H. Lee, C. F. Shu, F. I. Wu, and A. J. Carty, Orange and Red Organic Light-Emitting Devices Employing Neutral Ru (II) Emitters: Rational Design and Prospects for Color Tuning. *Adv. Funct. Mater.*, **16**(12), 1615 (2006).
13. D. F. Sava, L. E. Rohwer, M. A. Rodriguez, and T. M. Nenoff, Intrinsic broad-band white-light emission by a tuned, corrugated metal–organic framework. *J. Am. Chem. Soc.*, **134**(9), 3983 (2012).
14. A. F. Pozharskii, A. T. Soldatenkov, and A. R. Katritzky, *Heterocycles in life and society: an introduction to heterocyclic chemistry, biochemistry and applications*, John Wiley & Sons: 2011.
15. M. Sauer, J. Hofkens, and J. Enderlein, *Handbook of fluorescence spectroscopy and imaging: from ensemble to single molecules*, John Wiley & Sons: 2010.
16. G. L. Ingram and Z.-H. Lu, Design principles for highly efficient organic light-emitting diodes. *J. Photonics Energy*, **4**(1), 040993 (2014).
17. P. G. Schultz and X.-D. Xiang, Combinatorial approaches to materials science. *Current Opinion in Solid State and Materials Science*, **3**(2), 153 (1998).
18. H. Koinuma and I. Takeuchi, Combinatorial solid-state chemistry of inorganic materials. *Nat. Mater.*, **3**(7), 429 (2004).
19. I. Takeuchi, J. Lauterbach, and M. J. Fasolka, Combinatorial materials synthesis. *Mater. Today*, **8**(10), 18 (2005).
20. W. F. Maier, K. Stoewe, and S. Sieg, Combinatorial and high-throughput materials science. *Angew. Chem.*, **46**(32), 6016 (2007).
21. M. Mikami, Computational chemistry approach for white LED (oxy) nitride phosphors. *CS J. Solid State Sci. Technol.*, **2**(2), R3048 (2013).
22. D. Dutczak, T. Jüstel, C. Ronda, and A. Meijerink, Eu^{2+} luminescence in strontium aluminates. *Phys. Chem. Chem. Phys.*, **17**(23), 15236 (2015).
23. M. C. Maniquiz, K. Y. Jung, and S. M. Jeong, Luminescence Characteristics of $Y_3Al_{5-2y}(Mg, Si)_yO_{12}$: Ce Phosphor Prepared by Spray Pyrolysis. *J. Electrochem. Soc*, **157**(12), H1135 (2010).
24. P. Ghigna, S. Pin, C. Ronda, A. Speghini, F. Piccinelli, and M. Bettinelli, Local structure of the Ce^{3+} ion in the yellow emitting phosphor YAG: Ce. *Opt. Mater.*, **34**(1), 19 (2011).
25. P. Dorenbos, The 5d level positions of the trivalent lanthanides in inorganic compounds. *J. Lumin.*, **91**(3–4), 155 (2000).
26. P. Dorenbos, The $4fn \leftrightarrow 4f^{n-1}5d$ transitions of the trivalent lanthanides in halogenides and chalcogenides. *J. Lumin.*, **91**(1–2), 91 (2000).
27. I. A. Ibrahim, Z. Lenčéš, Ľ. Benco, M. Hrabalová, and P. Šajgalík, Sm-Doped $LaSi_3N_5$: Synthesis, Computed Electronic Structure, and Band Gaps. *J. Am. Ceram. Soc.*, **97**(8), 2546 (2014).
28. A. Watras, A. Matraszek, P. Godlewska, I. Szczygieł, J. Wojtkiewicz, B. Brzostowski, G. Banach, J. Hanuza, and P. Dereń, The role of the Ca vacancy in the determination of the europium position in the energy gap, its valence state and spectroscopic properties in $KCa(PO_3)_3$. *Phys. Chem. Chem. Phys.*, **16**(12), 5581 (2014).
29. X. Qin, X. Liu, W. Huang, M. Bettinelli, and X. Liu, Lanthanide-activated phosphors based on 4f-5d optical transitions: theoretical and experimental aspects. *Chem. Rev.*, **117**(5), 4488 (2017).
30. T. M. Tolhurst, P. Strobel, P. J. Schmidt, W. Schnick, and A. Moewes, Direct measurements of energy levels and correlation with thermal quenching behavior in nitride phosphors. *Chem. Mater.*, **29**(18), 7976 (2017).
31. P. Wagatha, V. Weiler, P. J. Schmidt, and W. Schnick, Tailoring Emission Characteristics: Narrow-Band Red Luminescence from SLA to $CaBa[Li_2Al_6N_8]:Eu^{2+}$. *Chem. Mater.*, **30**(21), 7885 (2018).
32. T. Vogt, P. Woodward, and B. Hunter, Prodjosantoso, A.; Kennedy, B., Sr_3MO_4F (M = Al, Ga)-A new family of ordered oxyfluorides. *J. Solid State Chem.*, **144**(1), 228 (1999).
33. A. Prodjosantoso, B. Kennedy, T. Vogt, and P. Woodward, Cation and anion ordering in the layered oxyfluorides $Sr_{3-x}A_xAlO_4F$ (A = Ba, Ca). *J. Solid State Chem.*, **172**(1), 89 (2003).
34. S. Park and T. Vogt, Luminescent phosphors, based on rare earth substituted oxyfluorides in the $A(1)_{3-x}A(2)_xMO_4F$ family with A (1)/A (2) = Sr, Ca, Ba and M = Al, Ga. *J. Lumin.*, **129**(9), 952 (2009).
35. S. Park and T. Vogt, Defect Monitoring and Substitutions in $Sr_{3-x}A_xAlO_4F$ (A = Ca, Ba) Oxyfluoride Host Lattices and Phosphors. *J. Phys. Chem. C*, **114**(26), 11576 (2010).
36. W. B. Im, K. Page, S. P. DenBaars, and R. Seshadri, Probing local structure in the yellow phosphor $LaSr_2AlO_5$: Ce^{3+}, by the maximum entropy method and pair distribution function analysis. *J. Mater. Chem.*, **19**(46), 8761 (2009).
37. H. S. Jang and D. Y. Jeon, Yellow-emitting Sr_3SiO_5: Ce^{3+}, Li^+ phosphor for white-light-emitting diodes and yellow-light-emitting diodes. *Appl. Phys. Lett.*, **90**(4), 041906 (2007).
38. H. S. Jang, H. Yang, S. W. Kim, J. Y. Han, S. G. Lee, and D. Y. Jeon, White light-emitting diodes with excellent color rendering based on organically capped CdSe quantum dots and Sr_3SiO_5: Ce^{3+}, Li^+ phosphors. *Adv. Mater.*, **20**(14), 2696 (2008).
39. H. Luo, J. Liu, X. Zheng, L. Han, K. Ren, and X. Yu, Enhanced photoluminescence of Sr_3SiO_5: Ce^{3+} and tuneable yellow emission of f Sr_3 SiO_5: Ce^{3+}, Eu^{2+} by Al^{3+} charge compensation for W-LEDs. *J. Mater. Chem.*, **22**(31), 15887 (2012).
40. P. P. Zhu, T. W. Huang, X. J. Wang, H. L. Li, and Z. Sun, In *Emission Color Variation of Sr_3SiO_5: Ce^{3+}, Li^+ Phosphor for Near-UV Light-Emitting Diodes by Co-Doping with Mg^{2+} and Ba^{2+}*, *Adv. Mater. Res., Trans Tech Publ*, 2013; pp 555.
41. M. Ando and Y. A. Ono, Temperature effects in the emission characteristics of CaS: Eu thin-film electroluminescent devices. *J. Cryst. Growth*, **117**(1–4), 969 (1992).
42. R. Green, M. Avdeev, and T. Vogt, Structural changes and self-activated photoluminescence in reductively annealed Sr_3AlO_4F. *J. Solid State Chem.*, **228**, 1 (2015).
43. Y. Fang, Y. Li, T. Qiu, A. Delsing, G. de With, and H. Hintzen, Photoluminescence properties and local electronic structures of rare earth-activated Sr_3AlO_4F. *J. Alloys Compd.*, **496**(1–2), 614 (2010).
44. H. Adachi, M. Tsukuda, and C. Satoko, Discrete variational Xα cluster calculations. I. Application to metal clusters. *J. Phys. Soc. Jpn.*, **45**(3), 875 (1978).
45. H. Yoshida, R. Yoshimatsu, S. Watanabe, and K. Ogasawara, Optical transitions near the fundamental absorption edge and electronic structures of $YAl_3(BO_3)_4$: Gd^{3+}. *Jpn. J. Appl. Phys.*, **45**(1R), 146 (2006).
46. M. Itoh and Y. Inabe, Optical properties and electronic structure of yttrium oxysulfide. *Phys. Rev. B*, **68**(3), 035107 (2003).
47. M. Shang, G. Li, X. Kang, D. Yang, D. Geng, and J. Lin, Tunable luminescence and energy transfer properties of Sr_3AlO_4F: RE^{3+} (RE = Tm/Tb, Eu, Ce) phosphors. *ACS Appl. Mater. Interfaces*, **3**(7), 2738 (2011).
48. M. Noh, S.-H. Cho, and S. Park, Tunable luminescence in Bi^{3+} and Eu^{3+} co-doped Sr_3AlO4_F Oxyfluorides phosphors. *J. Lumin.*, **161**, 343 (2015).
49. X. Zheng, H. Luo, J. Liu, P. Liu, and X. Yu, SrAlO F: Ce^{3+}-based yellow phosphors: structural tuning of optical properties and use in solid-state white lighting. *J. Mater. Chem. C*, **1**(45), 7598 (2013).
50. W. B. Im, N. N. Fellows, S. P. DenBaars, R. Seshadri, and Y.-I. Kim, $LaSr_2AlO_5$, a versatile host compound for Ce^{3+}-based yellow phosphors: structural tuning of optical properties and use in solid-state white lighting. *Chem. Mater.*, **21**(13), 2957 (2009).
51. W. B. Im, S. Brinkley, J. Hu, A. Mikhailovsky, S. P. DenBaars, and R. Seshadri, $Sr_{2.975-x}Ba_xCe_{0.025}AlO_4F$: a Highly Efficient Green-Emitting Oxyfluoride Phosphor for Solid State White Lighting. *Chem. Mater.*, **22**(9), 2842 (2010).
52. W. B. Im, N. George, J. Kurzman, S. Brinkley, A. Mikhailovsky, J. Hu, B. F. Chmelka, S. P. DenBaars, and R. Seshadri, Efficient and color-tunable oxyfluoride solid solution phosphors for solid-state white lighting. *Adv. Mater.*, **23**(20), 2300 (2011).
53. J. S. Lee, S. Unithrattil, and W. B. Im, Color-tunable binary solid-solution phosphor,$(Sr_3SiO_5)_{1-x}(Sr_3AlO_4F)_x$, for white LEDs: Energy transfer mechanism between Ce^{3+} and Tb^{3+}. *J. Alloys Compd.*, **555**, 297 (2013).
54. W. B. Im, Y. Fourré, S. Brinkley, J. Sonoda, S. Nakamura, S. P. DenBaars, and R. Seshadri, Substitution of oxygen by fluorine in the $GdSr_2AlO_5$: Ce^{3+} phosphors: $Gd_{1-x}Sr_{2+x}AlO_{5-x}$ Fx solid solutions for solid state white lighting. *Opt. Express*, **17**(25), 22673 (2009).
55. W. B. Im, N. N. Fellows, S. P. DenBaars, and R. Seshadri, $La_{1-x-0.025}Ce_{0.025}Sr_{2+x}Al_{1-x}Si_xO_5$ solid solutions as tunable yellow phosphors for solid state white lighting. *J. Mater. Chem.*, **19**(9), 1325 (2009).
56. K. A. Denault, N. C. George, S. R. Paden, S. Brinkley, A. A. Mikhailovsky, J. Neuefeind, S. P. DenBaars, and R. Seshadri, A green-yellow emitting oxyfluoride solid solution phosphor Sr_2 $Ba(AlO_4F)_{1-x}(SiO_5)_x$:$Ce^{3+}$ for thermally stable, high color rendition solid state white lighting. *J. Mater. Chem.*, **22**(35), 18204 (2012).
57. S. Unithrattil, H. J. Kim, and W. B. Im, Phase formation and luminescence properties of ternary solid-solution among tetragonal systems. *J. Alloys Compd.* (2019).
58. K. A. Denault, J. Brgoch, S. D. Kloß, M. W. Gaultois, J. Siewenie, K. Page, and R. Seshadri, Average and local structure, Debye temperature, and structural rigidity in some oxide compounds related to phosphor hosts. *ACS Appl. Mater. Interfaces*, **7**(13), 7264 (2015).
59. J. Brgoch, S. P. DenBaars, and R. Seshadri, Proxies from ab initio calculations for screening efficient Ce^{3+} phosphor hosts. *J. Phys. Chem. C*, **117**(35), 17955 (2013).